Differential spatial processing in ventral and lateral face-selective regions is scaffolded by structural connections

Authors

Dawn Finzi[1], Jesse Gomez[2,3], Marisa Nordt[1], Alex A. Rezai[1], Sonia Poltoratski[1], and Kalanit Grill-Spector[1,2,4]

[1] Department of Psychology, Stanford University, Stanford, CA

[2] Neurosciences Program, Stanford University, Stanford, CA

[3] Princeton Neuroscience Institute, Princeton University, NJ

[4] Wu Tsai Neurosciences Institute, Stanford University, Stanford, CA

Abstract

Face-processing occurs across ventral and lateral visual streams, which are involved in static and dynamic face perception, respectively. However, the nature of spatial computations across streams is unknown. Using functional MRI and novel population receptive field (pRF) mapping, we measured pRFs in face-selective regions. Results reveal that spatial computations by pRFs in ventral face-selective regions are concentrated around the center of gaze (fovea), but spatial computations in lateral face-selective regions extend peripherally. Diffusion MRI reveals that these differences are mirrored by a preponderance of white matter connections between ventral face-selective regions and foveal early visual cortex (EVC), while connections with lateral regions are distributed more uniformly across EVC eccentricities. These findings suggest a rethinking of spatial computations in face-selective regions showing that they vary across ventral and lateral streams, and further propose that spatial processing in high-level regions is scaffolded by the fine-grain pattern of white matter connections from EVC.

Introduction

Face perception is crucial for every day social interactions and relies on brain computations across a series of face-selective regions in occipital and temporal cortex. In humans, face-selective regions span two processing streams[1–4]: the ventral stream and the lateral stream[2]. The ventral face processing stream is thought to be involved in face categorization, recognition, and identification[5–9]. Cortically, it begins in early visual cortex (EVC: union of V1, V2, V3), continues to the inferior aspects of occipital and temporal cortex, and contains several face-selective regions: one on the inferior occipital gyrus (IOG-faces, also referred to as the occipital face area, OFA[10]), and two on the fusiform gyrus—one on the posterior fusiform (pFus-faces[11]) and one in the mid fusiform (mFus-faces[11])—which are collectively referred to as the fusiform face area (FFA[5]). These regions project[12] to an anterior temporal face patch[3]. The lateral face processing stream is thought to be involved in perception of dynamic[3,13,14], transient[15], and changeable aspects[7] of faces including motion[13,14,16,17], expression[7,8], and gaze[18,19]. This stream also emerges in early visual cortex and then continues to superior temporal cortex. It consists of a region in the posterior superior temporal sulcus (pSTS-faces[1,11]) and a region on the main branch of the STS (mSTS-faces[1,11]), then projecting to a region in the anterior STS (aSTS-faces[11,12,20]). Interestingly, pSTS-faces neighbors hMT+[21], an area involved in processing motion, and mSTS-faces neighbors regions that process biological motion[22,23]. As the ventral and lateral face processing stream are optimized for different tasks, a central open question is: what are the basic computations separating these streams?

The basic computation in the visual system is spatial processing performed by the receptive field[24] (RF), which is the region in visual space that is processed by a neuron. As neurons with overlapping RFs are clustered, we can measure the population receptive field (pRF)[25], i.e., the region in visual space processed by the collection of neurons in an fMRI voxel. Additionally, how a region spatially processes a stimulus depends on the way pRFs in the region tile the visual field[26]. This tiling is referred to as the visual field coverage (VFC) of the region. Therefore, we asked: what are the properties of pRFs and VFC in face-selective regions of the human ventral and lateral processing streams?

One possibility is that face-selective regions in both lateral and ventral streams perform similar spatial computations, and thus have similar pRF properties and VFC. As face perception requires the high visual acuity of central (foveal) vision, people tend to fixate on faces[27–30]. This habitual fixation on faces has led researchers to suggest that face-selective regions mainly process foveal information[31,32]. This hypothesis (Eccentricity Bias Theory[31]) is supported by findings that ventral face-selective regions respond more strongly to central than peripheral visual stimuli[31–33], and have a foveal bias, that is, denser coverage of the central than peripheral visual field[26,34]. In contrast, visual information related to other categories such as places, which in the real world occupy the entire visual field, extends to the periphery of the visual field irrespective of where people fixate. Supporting Eccentricity Bias Theory, researchers found that place-selective regions are peripherally-biased[32,33]. Thus, Eccentricity Bias Theory predicts that due to habitual fixation on faces, spatial processing in all face-selective regions, across ventral and lateral processing streams, will be foveally-biased.

An alternative hypothesis predicts that spatial computations may differ across face-selective regions in the ventral and lateral streams because these streams are optimized for different tasks with different computational demands. Specifically, face recognition, associated with the ventral stream, requires the fine spatial acuity afforded by central vision. This predicts that ventral face-selective regions that are involved in face recognition will have foveally-biased spatial computations[31,35]. In contrast, dynamic information in faces, which is associated with processing in lateral face-selective regions, requires fast temporal computations of transient visual information. As processing of visual information in the periphery is faster than in the fovea[15,36,37], spatial computations in lateral face-selective regions may extend to the periphery.

To test these hypotheses, we designed a novel pRF mapping experiment optimized to map pRFs in high-level visual regions (**Figure 1a**). Using these data, we estimated pRFs in each voxel and then compared pRFs and VFC across face-selective regions in the ventral and lateral streams.

We also considered an important, related question: how do spatial processing characteristics and eccentricity biases emerge in high-level visual regions in the first place? A prevalent view suggests that the hierarchical organization of visual processing streams, as well

as pooling operations from one stage to the next, generate successively larger pRFs in higher-level stages of the processing hierarchy[38,39]. Indeed, large pRFs in the end stages of the processing hierarchy may be optimized to process whole stimuli such as faces[40]. This hierarchical organization may be supported by sequential connections along regions constituting the processing steam[12,40,41]. However, other evidence shows that the human visual stream is not strictly hierarchical[41–43] as there are skip connections[40] between areas that are not consecutive in the hierarchy. In fact, recent studies report the existence direct white matter connections between EVC and face-selective regions of both lateral and ventral processing streams[41,42], which may enable fast visual processing[44].

However, the nature of direct connections from early stages of the visual hierarchy to later stages and how they relate to spatial processing in downstream regions remains a mystery. As EVC has a topographic representation of visual space, we examined the pattern of white matter connections between specific eccentricity bands in EVC and face-selective regions. We reasoned that to support large pRFs in high-level regions, there should be connections between a range of EVC eccentricities and face-selective regions. However, we hypothesized that one source of emergent spatial biases in face-selective regions could be an uneven distribution of connections emerging from central and peripheral eccentricities in EVC. That is, we predicted that regions that are foveally-biased will have a preponderance of white matter tracts emerging from central compared to peripheral eccentricities of EVC. In contrast, regions in which spatial processing extends to the periphery will have a more uniform distribution of connections across EVC eccentricities. We tested these predictions in a second experiment, in which we used diffusion MRI (dMRI) and fMRI in the same participants to determine the distribution of white matter tracts between EVC eccentricity bands and each of the face-selective regions.

Results

"Toonotopy" (retinotopy with cartoons) drives responses in face-selective cortex more than standard checkerboard retinotopy

To measure pRFs, 21 adults (10 female) participated in a wide-field pRF mapping experiment which used colorful cartoon images ("toonotopy", **Figure 1A**). In the experiment, subjects fixated on a central dot, and pressed a button when it changed color. As they performed this task, they

viewed a bar extending 40° in length that systematically swept the visual field (**Figure 1a**). Unlike standard pRF mapping[25,34] that uses flickering checkerboards, our bars contained random images from cartoons including colorful faces, objects, scenes, and text presented at a rate of 8Hz. Additionally, subjects participated in a 10-category localizer experiment[45] to independently define their face-selective regions.

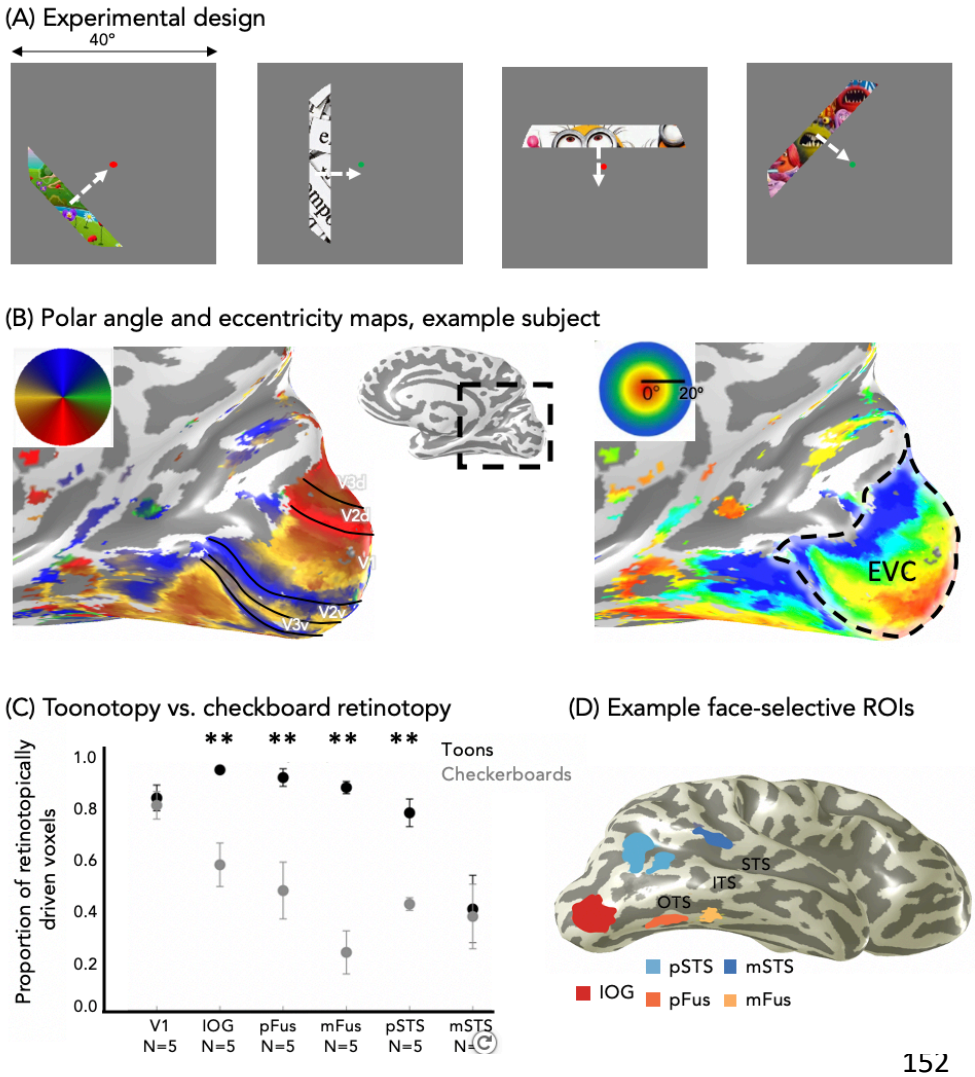

Figure 1. Toonotopy experiment and regions of interest. (A) Experimental design. A bar containing colored cartoon images changing at 8 Hz is swept across a gray background in 4 orientations (0°, 45°, 90°, 135°), each in 2 directions orthogonal to the bar. Each sweep takes 24 seconds, with blanks after six bar steps (12 seconds) for each diagonal direction. Participants were instructed to fixate and indicate when the fixation dot changed color. (B) Example polar angle (left) and eccentricity (right) maps in a representative participant's inflated right hemisphere. *Inset:* zoomed medial view. Maps are thresholded at 10% variance explained, voxel level. *Solid lines:* boundary of retinotopic areas. *Dashed contour:* early visual cortex: union of V1, V2 and V3. (C) Proportion of voxels in each right hemisphere region in which pRF model explains >10% of their variance. Data averaged across five participants who underwent both checkerboard retinotopy and toonotopy. *Error bars*: ±SE (standard error of the mean). Asterisks indicate significant differences between toonotopy vs. checkerboard retinotopy; post-hoc Tukey t-tests (** $p < .01$) (D) Face-selective regions defined from the localizer experiment in a representative participant's inflated right hemisphere using contrast: faces vs. all other categories, $t>3$, voxel level. *Warm colors: v*entral face-selective regions; *Cold colors*: lateral face-selective regions. *Acronyms*: *IOG:* inferior occipital gyrus; *pFus:* posterior fusiform. *mFus:* mid fusiform; *OTS:* occipito-temporal sulcus; *ITS:* inferior temporal sulcus; *STS:* superior temporal gyrus.

From the localizer experiment, we defined three ventral face-selective regions (IOG, pFus, mFus-faces) and two lateral face-selective regions (pSTS, mSTS-faces) in each subject's brain (**Figure 1D**, Methods). Additionally, we defined in each participant their ventral place-selective region (CoS-places), which we include to replicate prior findings and as a control in certain analyses. All regions were found bilaterally except for mSTS-faces, which was lateralized to the right hemisphere in all but six participants. Due to the lack of mSTS-faces in the left hemisphere, as well as the vast literature reporting lateralization of face-selectivity[3,46], we analyze data from each hemisphere separately throughout this study, unless otherwise specified.

In the toonotopy pRF mapping experiment, we used colorful cartoon stimuli and fast presentation rates in an attempt to maximally drive responses in high-level visual cortex. To quantify the success of this approach, in five participants we compared toonotopy to a standard checkerboard pRF mapping experiment, which was identical to the toonotopy experiment except the bars contained black and white checkerboards that flickered at a rate of 2Hz. In each participant and experiment, we fit a pRF for each voxel and identified the voxels for which the pRF model explained at least 10% of their variance.

Qualitatively, toonotopy pRF mapping yielded the typical retinotopic polar angle and eccentricity maps (**Figure 1B**). Along the calcarine we found a hemifield representation, corresponding to V1, followed by mirror reversals of the polar angle (**Figure 1B**-left). Likewise, we found the standard eccentricity map of the occipital lobe, with foveal representations close to the occipital pole, and systematically more peripheral eccentricities proceeding from posterior to anterior along the calcarine sulcus (**Figure 1B**-right). Using the polar angle map, we defined in each subject V1, V2, V3 and their union (referred to as early visual cortex: EVC, **Figure 1B**-right).

Quantitatively, we compared the amount of retinotopically-modulated voxels across experiments. Differences between the ability of mapping stimuli to drive high-level face-selective regions are striking. Nearly 90% of mFus-faces voxels in the right hemisphere were driven in the toonotopy experiment, compared to less than 25% in the checkboard experiment (**Figures 1C, S1-**left hemisphere). As linear mixed models (LMMs) tolerate missing values[47] (e.g. when there are missing regions of interest (ROIs)), here and in subsequent analyses, we applied LMMs to analyze the data. The significance of fixed effects in these models were evaluated using analyses-

191 of-variance with Satterthwaite approximations for degrees of freedom[48] (referred to as LMM
192 ANOVA). A 2-way repeated measures LMM ANOVA on the proportion of retinotopically-driven
193 voxels with factors of experiment (toonotopy/checkerboards) and ROI
194 (V1/IOG/pFus/mFus/pSTS/mSTS) revealed a significant ROI x experiment interaction in both the
195 right ($F(5, 44)=5.0$, $p=.0010$) and left hemispheres ($F(5, 40)=3.9$, $p=.0057$) as the type of mapping
196 experiment had a pronounced effect on driving responses in face-selective regions, but not V1
197 (**Figures 1C, S1**).
198
199 *pRF centers in ventral face-selective ROIs have a foveal bias while pRFs in lateral face-selective*
200 *regions extend to the periphery*
201 Next, we compared pRF characteristics across ventral and lateral face-selective ROIs. Visualizing
202 pRF centers across participants for each ROI (**Figure 2A**) reveals differences across ventral and
203 lateral regions. pRF centers of ventral face-selective regions, IOG, pFus and mFus, are largely
204 confined within the central 10° (**Figures 2, S2**). In contrast, pRF centers of lateral face-selective
205 regions, pSTS and mSTS, extend to the periphery, even past 30° from fixation. Notably, the
206 distribution of pRF centers of pSTS-faces is more similar to CoS-places, a ventral place-selective
207 region with a peripheral bias[33], than to ventral face-selective regions.
208 We quantified these observations by calculating the proportion of pRF centers within
209 each of four eccentricity bands (0–5°/5–10°/10–20°/20–40°) for each participant and ROI (**Figure**
210 **2B**). These eccentricities bands were chosen as they approximately occupy a similar cortical
211 expanse due to cortical magnification[25,49]. As illustrated in **Figure 2B**, the foveal bias is particularly
212 striking in the right hemisphere, where ~70% of pRF centers in right ventral face-selective regions
213 are located within the central 5° (right IOG-faces: mean±SE=0.71±0.07; pFus-faces: 0.69±0.06;
214 mFus-faces: 0.76±0.06), with very few pRF centers located outside the central 10°.
215 Lateral face-selective ROIs show the opposite distribution of pRF centers across
216 eccentricity bands. In these regions, the proportion of centers increases from central to
217 peripheral eccentricity bands. In stark contrast to ventral face-selective ROIs, less than 20% of
218 centers were located within the central 5° eccentricity band for lateral face-selective regions

(right pSTS-faces: 0.15±0.05; right mSTS-faces: 0.16±0.11). Here, the majority of pRF centers are outside the central 10°.

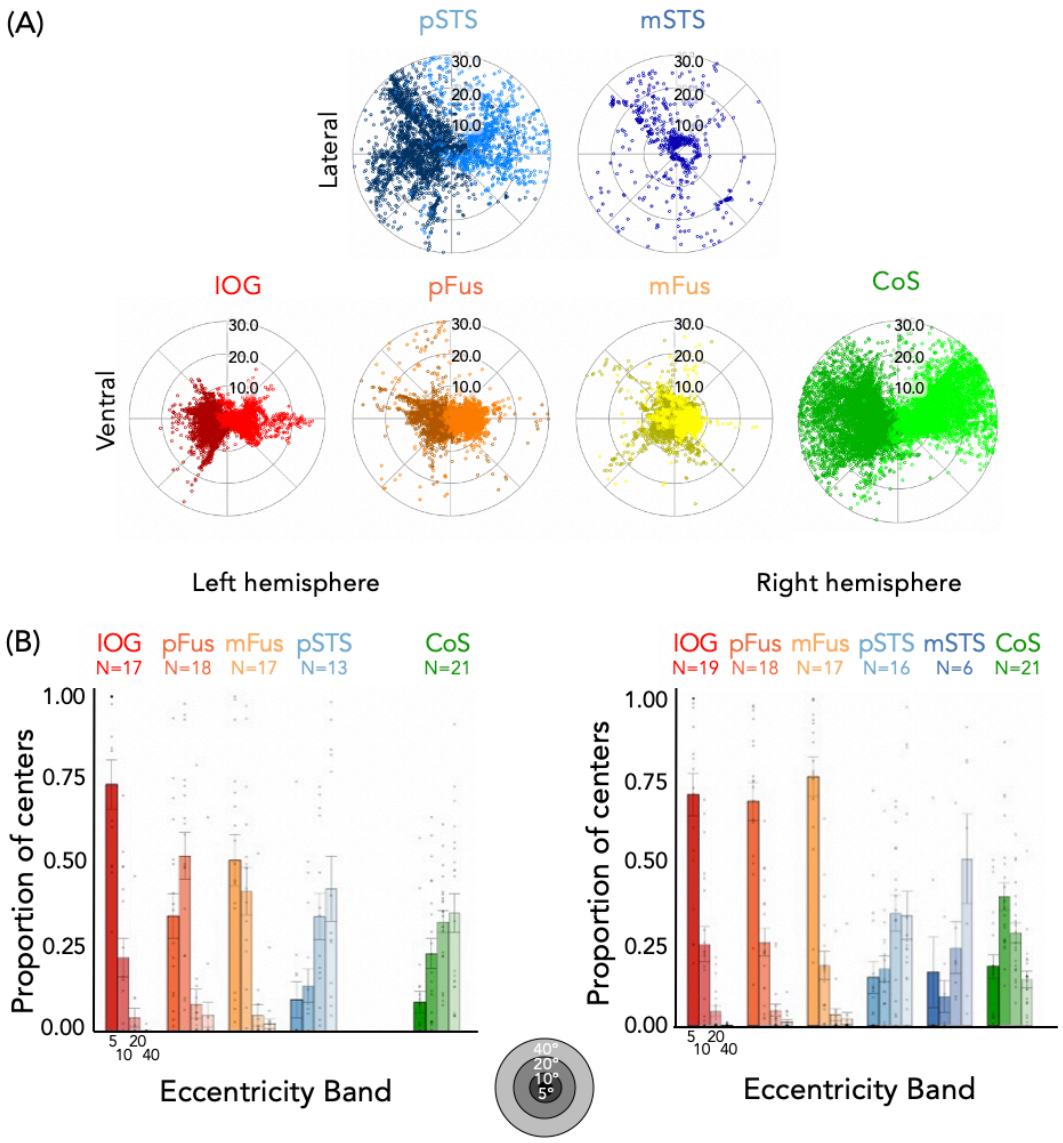

Figure 2. pRF centers in ventral face-selective ROIs have a foveal bias, while pRF centers in lateral face-selective regions (and CoS-places) extend to the periphery. (A) Distribution of pRF centers; Each dot is a pRF center. *Dark colors:* Right hemisphere. Left mSTS-faces is not shown as it could only be localized in three participants. (B) *Bars:* mean proportion of pRF centers of face-selective ROIs and CoS-places across eccentricity bands (0°–5°, 5°–10°, 10°–20°, and 20°–40°) averaged across participants. *Error bars*: ±SE. *Dots:* individual participants.

A 2-way repeated measures LMM ANOVA on the proportion of centers with eccentricity band (0–5°/5–10°/10–20°/20–40°) and stream (ventral: IOG/pFus/mFus and lateral: pSTS/mSTS; mSTS, right hemisphere only) as factors revealed a significant eccentricity band x stream interaction in both hemispheres (right: $F(3, 304)=80.8$, $p<2.2x10^{-16}$; left: $F(3,256)=30.1$, $p=2.2x10^{-}$

[16]). Post-hoc Tukey's tests establish that this is driven by a significantly higher proportion of centers in the most foveal 0–5° eccentricity band in ventral vs. lateral face-selective regions (proportion higher in ventral than lateral 0–5°: right: 0.56±0.05 , $t(304)=12.0$, $p<.0001$; left: 0.43±0.07, $t(256)=5.9$, $p<.0001$), as well as a significantly lower proportion of centers for ventral vs. lateral regions in the two most peripheral eccentricity bands (proportion lower in ventral than lateral, 10–20° right: 0.27±0.05, $t(304)=-5.7$, $p<.0001$; left: 0.29±0.07, $t(256)=-3.9$, $p=.0001$; 20–40° right: 0.38±0.05, $t(304)=-8.0$, $p<.0001$; left: 0.40±0.07, $t(256)=-5.4$, $p<.0001$). Additionally, differences in pRF center distributions are not a general characteristic of ventral vs. lateral regions, as CoS-places, which is a ventral region, has pRFs that extend into the far periphery (**Figure 2-**green).

There were also significant differences in the distribution of pRF centers between hemispheres in ventral face-selective ROIs, revealed by a significant hemisphere by band by ROI interaction ($F(6, 400)=5.0$, $p<6.2x10^{-5}$, 3-way repeated measures LMM ANOVA with factors of hemisphere, eccentricity band, and ROI) and a significant hemisphere by band interaction ($F(3, 400)=13.7$, $p<1.6x10^{-8}$). As evident in **Figure 2B,** pRF centers were concentrated more foveally in the right hemisphere than in the left, particularly in pFus-faces and mFus-faces. For both pFus-faces and mFus-faces, there were significantly more pRF centers in the 0°–5° band in the right than left hemisphere (proportion of pRFs in the 0°–5°: pFus-faces - right: mean±SE=0.69±0.06; left: 0.34±0.07; post-hoc Tukey test $t(400)=-5.2$, $p<.0001$; mFus-faces - right: mean±SE=0.76±0.06; left: 0.51±0.08; post-hoc Tukey test $t(400)=-3.7$, $p=.0002$).

Together this analysis reveals (i) differences in distribution of pRF centers across face-selective regions of the lateral and ventral streams, and (ii) a higher foveal bias in right than left ventral face-selective regions.

pRFs in lateral face-selective ROIs are larger than pRFs in ventral face-selective regions

In addition to differences in pRF locations, pRF sizes differ between lateral and ventral face-selective regions. Specifically, median pRF sizes are larger in lateral than ventral face-selective regions (**Figure 3A**). In the right hemisphere, for example, the average across participants of median pRF sizes in pSTS faces was 21.7°±1.3°, while in pFus-faces (the ventral region with the

largest pRFs) the average was 9.4°±1.2°. To determine if these differences were significant, we calculated in each participant the median pRF size across ROIs in each stream (ventral: IOG/pFus/mFus and lateral: pSTS/mSTS; mSTS, right hemisphere only) and then compared values across streams. Results show that in both hemispheres pRFs were significantly larger in lateral than ventral face-selective regions (paired t-tests; right: t(16)=-5.5, p=4.8x10^{-5}; left: t(13)=-5.8, p=5.8x10^{-5}). Differences between ROIs were significant (1-way repeated measures LMM ANOVAs on median pRF size, right ROIs: IOG/pFus/mFus/pSTS/mSTS, F(4,60)=25.1, p=3.6x10^{-12}; left ROIs: IOG/pFus/mFus/pSTS, F(3,46)=27.9, p=2.1x10^{-10}), and were driven by significant differences between pSTS-faces and each of the ventral face-selective regions (post-hoc Tukey tests, all *ts*>5.9, *ps*<.0001, **Table S1**).

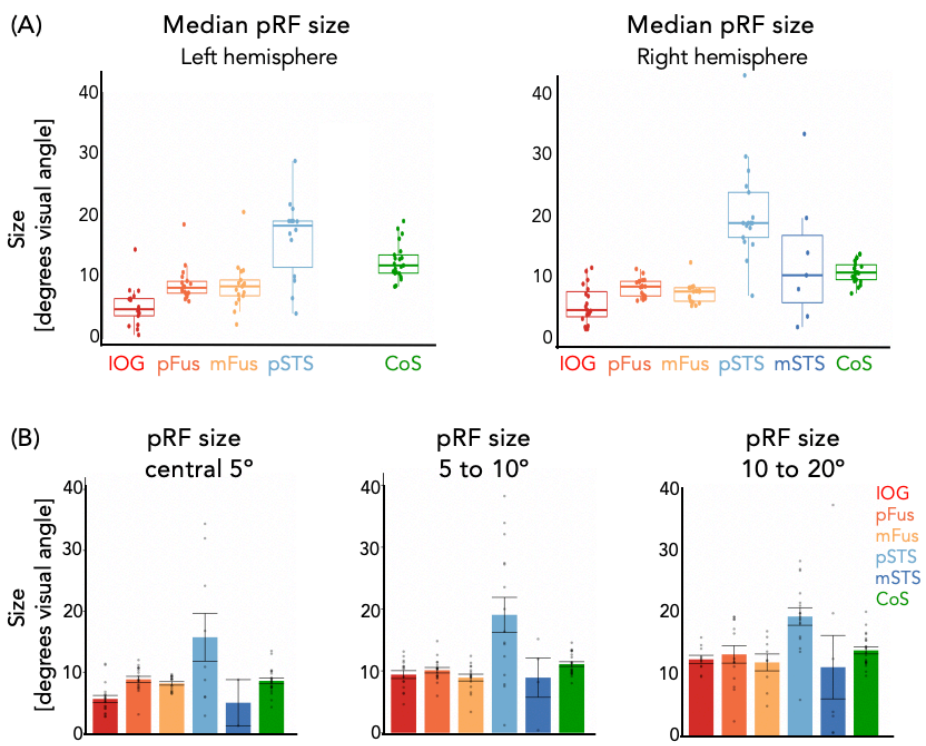

Figure 3. pRFs in lateral face-selective regions are larger than in ventral face-selective regions. (A) Median pRF size ($\frac{\sigma}{\sqrt{n}}$) in face-selective regions and CoS-places. *Box:* median and 25%, 75% percentiles; *lines:* ±1.5 times interquartile range; *Dots:* individual participant median pRF size. (B) Average median pRF size across participants for each eccentricity band of right hemisphere regions. Left hemisphere ROIs were not included as we could only identify in 5 participants any voxels whose pRF eccentricity was less than 5º in any of the lateral ROIs. *Dots:* Individual participant median pRF size. *Error bars*: ±SE.

As pRF size increases with eccentricity in retinotopic regions[25], we next tested if differences in pRF sizes across pSTS and ventral regions were simply driven by the higher number of peripheral pRFs in the former than the latter. We reasoned that if that were the case, then comparison of pRF sizes within the same eccentricity band should reveal no difference across

301 ROIs. However, comparison of pRF sizes within the same eccentricity band revealed significant
302 differences between median pRF across ROIs (**Figure 3B,** 1-way LMM ANOVAs with factor of ROI,
303 right hemisphere, 0–5° band: $F(4,62)=6.8$, $p=.00013$; 5–10° band: $F(4,53)=8.7$, $p=1.9\times10^{-5}$).
304 Moreover, across both the 0–5° and 5–10° bands, pRFs were significantly larger in right pSTS-
305 faces than in any other region except mSTS-faces (all *t*s>4.1, *p*s<=.0012, **Table S2**). We note that
306 pRF size in pSTS faces did not increase much with eccentricity, consistent with prior studies[50].
307
308 *Ventral face-selective ROIs have dense coverage of the central visual field, while lateral face-*
309 *selective ROIs have coverage that extends to the periphery*
310 How do differences in pRF locations and sizes across face-selective ROIs affect their visual field
311 coverage (VFC)? VFC was calculated as the proportion of pRFs covering each point in the visual
312 field, for each participant and ROI, then averaged across subjects. Results reveal three main
313 findings illustrated in **Figure 4A**: (1) In all ROIs, VFC is concentrated in the contralateral visual field
314 (see also **Figure S3**), (2) ventral face-selective ROIs have dense coverage concentrated around
315 the center of the visual field, and (3) lateral face-selective ROIs have more diffuse coverage that
316 extends further into the periphery than in ventral face-selective ROIs. These differences are not
317 a general characteristic of ventral vs. lateral regions, as ventral CoS-places exhibits VFC that
318 extends into the periphery.
319 To quantify differences in VFC, we calculated average pRF density as a function of
320 eccentricity for the contralateral visual field of each ROI. Ventral face-selective regions displayed
321 high pRF density close to the fovea that decreased sharply beyond ~10°, while pRF density in
322 lateral face-selective regions decreased more moderately with increasing eccentricity (**Figure**
323 **4B**). We summarized the relationship between pRF density and eccentricity by fitting a line for
324 each participant's pRF density curve per ROI. Negative slopes indicate higher pRF density near
325 the fovea than periphery, and slopes close to 0 indicate similar pRF densities across eccentricities.
326 Results reveal (i) significant differences between the average slopes of ventral and lateral face-
327 selective regions (paired t-tests; right: $t(16)=-9.4$, $p=6.9\times10^{-8}$; left: $t(13)=-5.2$, $p=.00016$), whereby
328 slopes for ventral face-selective ROIs were more negative than for lateral face-selective ROIs and
329 (ii) significant differences between the average slopes of individual face-selective ROIs (right:

F(4,58)=56.8, $p<2.2x10^{-16}$; left: F(362)=16.3, $p=6.1x10^{-8}$, 1-way repeated measures LMM ANOVAs on the slopes with factor ROI). Specifically, slopes in lateral face-selective regions—pSTS-faces and mSTS-faces—were significantly closer to zero than any of the ventral face-selective regions (all *ts*>3.7, *ps*<=.0022, post-hoc Tukey tests, **Table S3**). Additionally, bilateral pFus-faces and right mFus-faces had significantly more negative slopes than IOG-faces (all *ts*<-3.1, *ps*<=.017, **Table S3**), indicating that the former ROIs have a larger foveal bias than the latter.

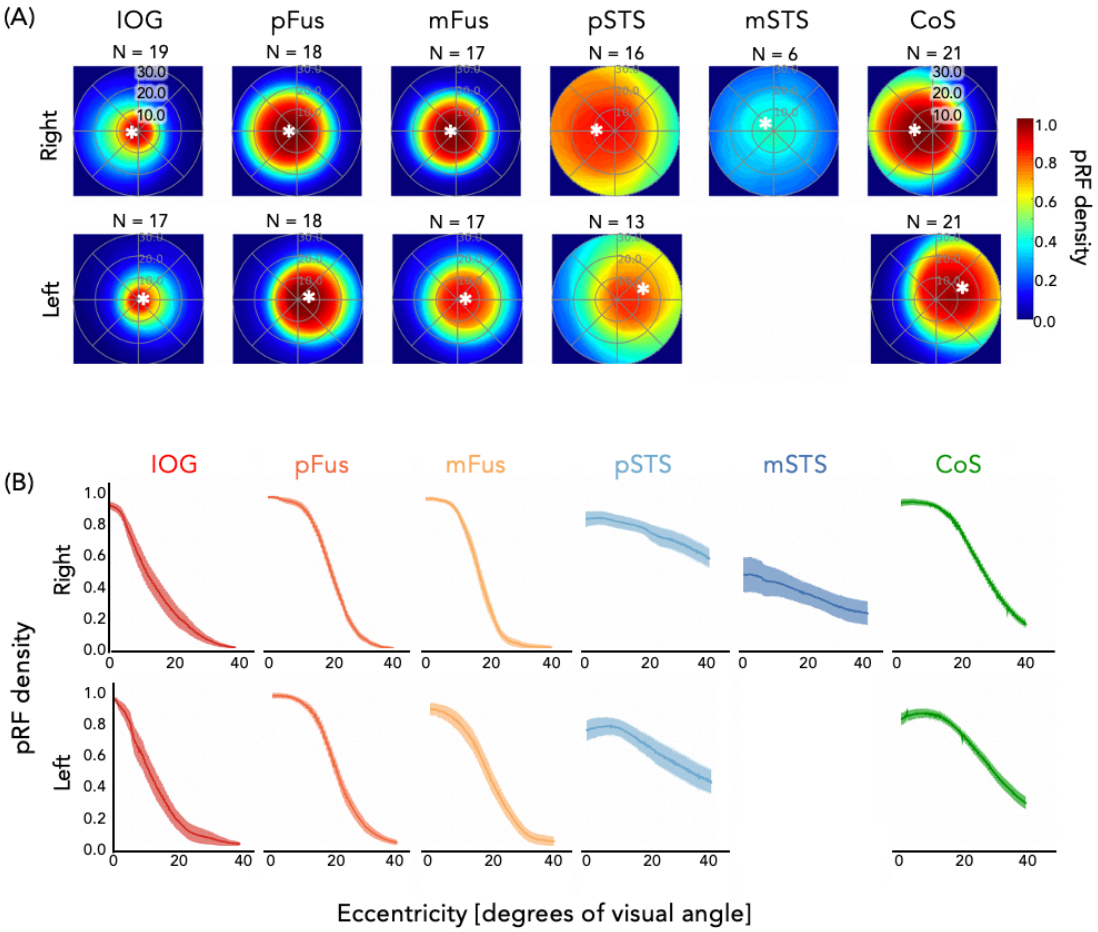

Figure 4. Dense coverage of the central visual field in ventral face-selective regions, but coverage extends to the periphery in lateral face-selective regions (and CoS-places). (A) Average visual field coverage of each ROI across participants (number indicated above each plot). Visual field coverage is computed as the proportion of pRFs covering each point in the visual field for each participant and then averaged across participants. *Asterisk:* average location of the center of mass of all pRF centers in each ROI; (B) Average pRF density as a function of eccentricity for the contralateral visual field of each ROI. Data were calculated per participant and then averaged across participants. *Shaded area:* standard error of the mean.

Face-selective regions have direct white matter connections to early visual cortex

Given our findings of differences in pRF properties and visual field coverage across ventral vs. lateral face-selective regions, we asked how white matter connections from early visual cortex (EVC) contribute to this differentiation. We reasoned that the foveal bias in ventral face-selective regions may arise in part from a preponderance of connections from foveal eccentricities of EVC. In contrast, the more uniform tiling of the visual field by pRFs in lateral face-selective regions may rise from a more uniform pattern of white matter connections from EVC eccentricities to these face-selective ROIs along the STS.

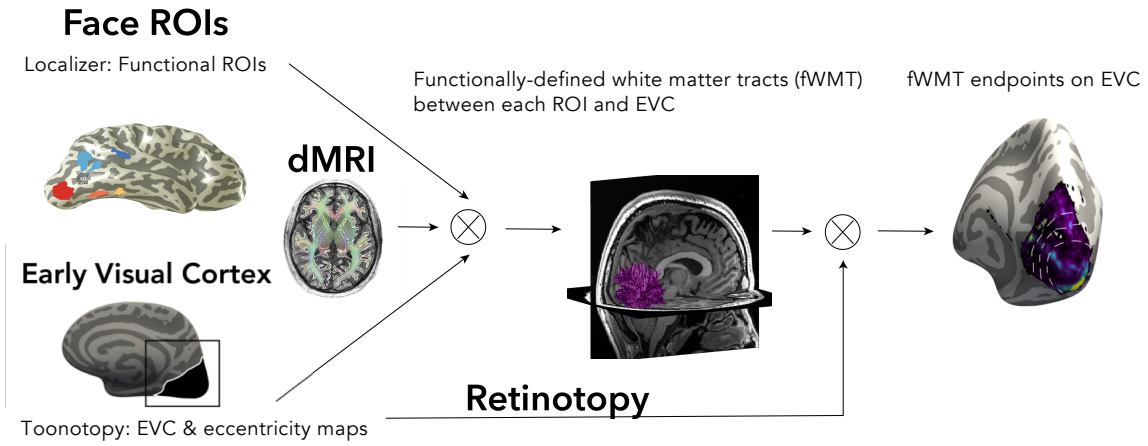

Figure 5. Functionally-defined white matter tracts (fWMT) between functional ROIs and early visual cortex (DVC). We combined dMRI and fMRI in each participant to determine fWMT between each functional ROI and EVC. *From left to right: fMRI:* from the localizer experiment, we defined in each participant their face-selective ROIs; from the toonotopy experiment, we defined in each subject their EVC and eccentricity map. *dMRI:* using MRTrix3 with ACT we defined the whole brain connectome of each participant, which was culled to remove false alarm tracts with Linear Fascicle Evaluation{ref}. *fWMT of each ROI:* all tracts that intersect with both the functional ROI and EVC. *Endpoints in EVC*: We projected the end points of each fWMT in EVC and related it to the eccentricity map. All analyses were done in each participant's native brain space.

To test these predictions, we acquired an additional diffusion-weighted MRI (dMRI) scan from 16 of our participants (see Methods). We combined dMRI data with the fMRI data from both localizer and toonotopy experiments to identify the functionally-defined white matter tracts (fWMT) that connect each face-selective region with EVC (**Figure 5**). We used anatomically-constrained tractography (ACT)[51], which uses the gray-white matter-interface to seed the tractography. This guarantees that the resulting fiber tracts reach the gray matter, which is crucial for testing our hypothesis. As a control, we also defined the fWMT that connect CoS-places with

EVC. We asked: (1) Are there white matter tracts that connect each of the face-selective ROIs and EVC? (2) If so, how are they distributed across EVC eccentricities?

We found direct white matter connections between each face- and place-selective region and EVC in all participants where we could localize the region (**Figure 6A**, representative subjects; all subjects, **Supplementary Figure S4**). Qualitatively, fWMT between face-selective regions and EVC were largely consistent across participants, although the proportion of tracts varied substantially by region (**Figure 7B**). IOG-faces had the highest percentage of its tracts connecting to EVC (right: mean±SE=37.7±2.9%, left: 39.6±3.1%), followed by pFus-faces (right: 13.2±1.7%, left: 14.7±2.8%). mSTS-faces had the lowest percentage, with less than 3% of all mSTS-faces tracts connecting to EVC (right: 2.1±0.6%; left: 2.6±0.9%). However, in both hemispheres, ventral mFus-faces and lateral pSTS-faces had similar percentages of tracts to EVC (right mFus-faces: 9.5±1.6%, left mFus-faces: 8.4±0.9%; right pSTS-faces: 10.8±1.7%, left pSTS-faces: 9.0±1.6%), suggesting that differences in fWMT to EVC do not stem from differences in our ability to identify tracts across ventral and lateral streams. Additionally, despite their adjacent locations, ventral regions mFus-faces and CoS-places have different percentages of connections to EVC. Specifically, CoS-places has twice the percentage of connections to EVC as mFus-faces (right: 22.0±2.9%; left: 17.4±3.1%). These data further underscore that factors other than anatomical location determine the percentage of tracts between functional ROIs and EVC.

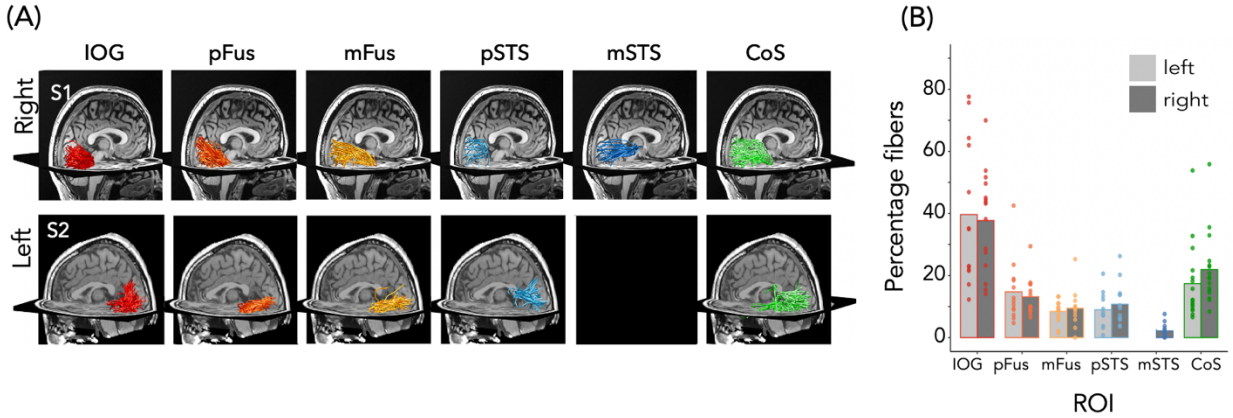

Figure 6. White matter tracts connecting EVC and face-selective regions (and CoS-places). (A) *Top:* right hemisphere, Subject 1; *Bottom:* left hemisphere, Subject 2. (B) Mean percentage of fWMT between each functional ROI and EVC. 100% indicates that all tracts starting at an ROI connect to EVC and 0 indicates that no tracts connect to EVC. Percentage is calculated for each participant (circles) and then averaged across participants (bars). *Lighter bars*: left hemisphere; *Darker bars:* right hemisphere.

Ventral and lateral face-selective regions differentially connect to EVC eccentricities

To test whether ventral and lateral face-selective regions are differentially connected to EVC eccentricities, we evaluated to which eccentricity band in EVC these tracts connect. Eccentricity values were determined from each participant's toonotopy data. We then quantified what proportion of tracts from an ROI to EVC connected to each of four EVC eccentricity bands: 0–5°, 5–10°, 10–20°, 20–40° (**Figure 7**).

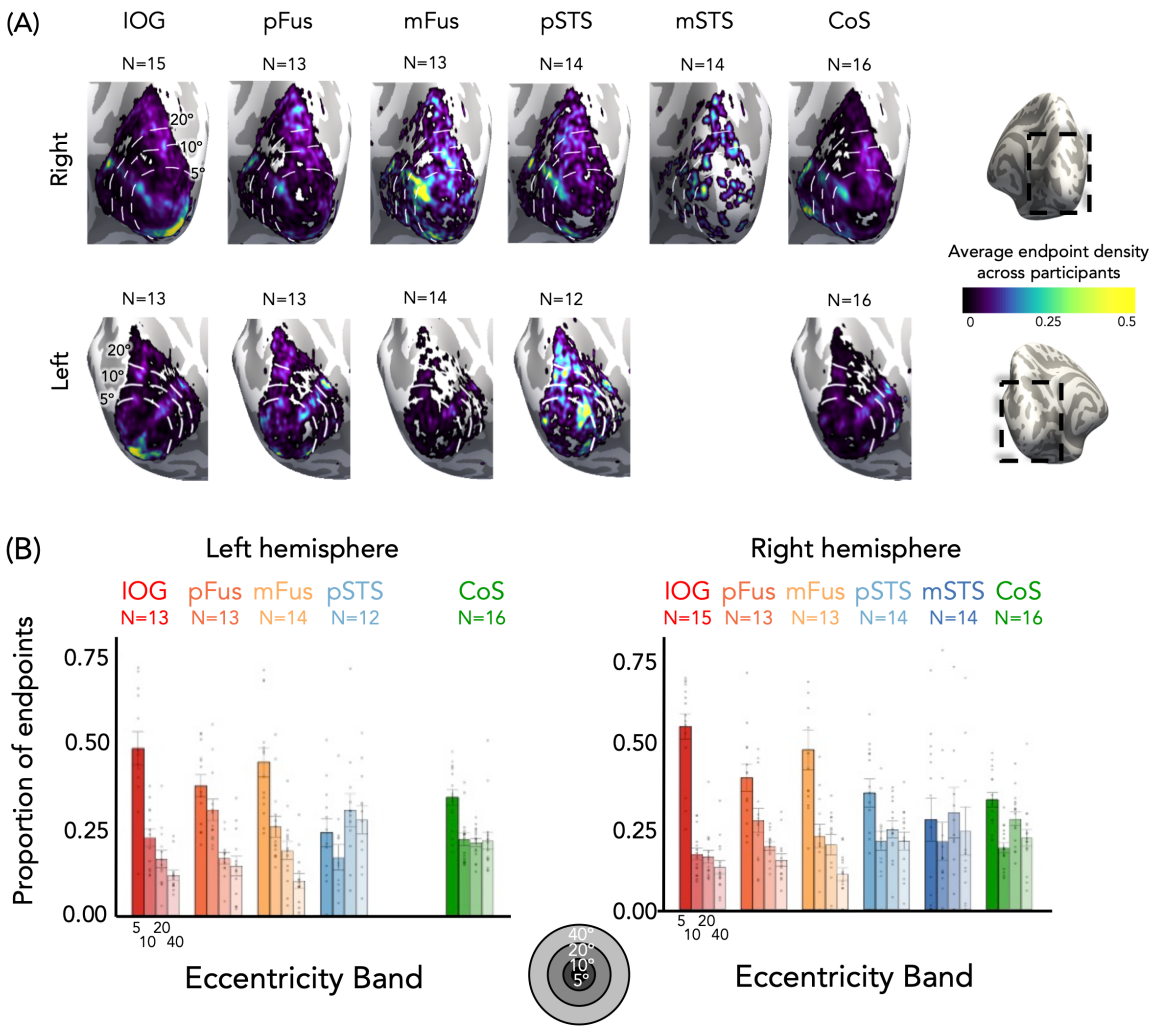

Figure 7. Tracts from lateral and ventral face-selective regions have a different distribution across early visual cortex (EVC) eccentricities. (A) Mean endpoint density of fiber tracts connecting each ROI with EVC shown on the zoomed medial inflated cortical surface of the FreeSurfer average brain; *Top:* right hemisphere; *Bottom:* left hemisphere. *Color map:* average density across participants. Eccentricity bands (white) were derived from the average of all participants' retinotopies. (B) Average proportion of tract endpoints from each ROI that terminate in each of four EVC eccentricity bands (0°–5°; 5°–10°; 10°–20º°; 20°–40°). *Bars:* mean across participants; Each dot is a participant; *Error bars*: ±SE. Analyses done in native subject brain space

410 For ventral face-selective regions in both hemispheres, the highest proportion of white
411 matter endpoints were located within the central 5° of EVC, while the fewest endpoints were
412 within the most peripheral EVC eccentricity band, mirroring the results for pRF centers (**Figure**
413 **7A**, IOG, pFus, mFus). In fact, the majority (>66%) of the tracts connecting EVC to ventral face-
414 selective ROIs originate within the central 10°. This overrepresentation of tract endpoints within
415 the central EVC is not the case for lateral face-selective regions. In these regions, tract endpoints
416 are instead more evenly distributed across EVC eccentricity bands, with at least 20% of endpoints
417 in the most peripheral eccentricity band (>40°, **Figure 7A**-pSTS, mSTS). Importantly, this
418 difference is not due to a general bias that favors connections from foveal eccentricities in EVC
419 to VTC, as the tracts that connect to ventral CoS-places to EVC are more uniformly distributed
420 across EVC eccentricities. In fact, nearly half of the tracts from EVC to CoS-places (right: 48%, left:
421 43%) originate in eccentricities ≥20° .
422 To test the significance of endpoint distributions in EVC between streams, we ran a 2-way
423 repeated-measures LMM ANOVA on the proportion of tract endpoints in EVC with factors of
424 eccentricity band (0–5°/5–10°/10–20°/20–40°) and stream (ventral: IOG/pFus/mFus and lateral:
425 pSTS/mSTS; mSTS right hemisphere only). We found a significant eccentricity band x stream
426 interaction in both hemispheres (right: F(3, 268)=10.3, p=2.0x10^{-6}; left: F(3,200)=19.5, p=3.8x10^{-}
427 ^{11}). As with the proportion of pRF centers, post-hoc Tukey's tests establish that stream
428 differences are driven by a significantly higher proportion of tract endpoints in the most central
429 eccentricity band (0–5°) in ventral vs. lateral face-selective regions (proportion higher in ventral
430 than lateral, right: 0.17±0.04, t(268)=4.4, p<.0001; left: 0.20 ± 0.04, t(200)=5.0 p<.0001), as well
431 as a significantly lower proportion of centers for ventral vs. lateral regions in the two most
432 peripheral eccentricity bands (proportion lower in ventral than lateral, 10–20°, right: 0.09±0.04,
433 t(268)=-2.2, p=.0253; left: 0.13±0.04, t(200)=-3.4, p=.0009; 20–40°, right: 0.09±0.04, t(268)=-2.5,
434 p=.0148; left: 0.16±0.04, t(200)=-4.0, p=.0001). To control for any effects of ROI size, we repeated
435 this analysis with 5 mm disk ROIs, created at the center of each functionally defined region
436 (**Supplementary Figure S5**). As in the main analysis, a 2-way repeated-measures ANOVA on the
437 proportion of fiber endpoints in EVC confirms significant eccentricity band x stream interactions
438 in both hemispheres (right: F(3, 256) = 8.7, p = 1.65 x 10^{-5}; left: F(3,200) = 17.3, p = 5.248 x 10^{-10}).

Together, we find that the ventral and lateral face-selective regions differentially connect to EVC. Ventral face-selective regions connect more to central eccentricity bands in EVC, while lateral face-selective regions show connections that are distributed across eccentricity bands and extend into the far periphery. White matter connectivity differences between ventral and lateral face-selective ROIs echo the different distributions of pRF centers, suggesting that white matter connections may provide a scaffolding for differential spatial processing between streams.

Discussion

Using a multimodal approach, we tested how different face-selective regions of visual cortex represent visual space and whether this can be traced to white matter connections with early visual cortex. We find that (i) contrary to the prevailing view, not all face-selective regions are foveally biased, as lateral face-selective regions show visual field coverage extending into the far periphery, and that (ii) these differences are reflected in differential patterns of white matter connections with EVC, as lateral face-selective regions exhibit white matter connections that are more evenly distributed across eccentricities than ventral face-selective regions.

Consistent with prior research illustrating a foveal bias in face-selective regions[32,33,52], our data show that pRF properties and VFC of ventral occipital and temporal face-selective regions process information around the center of gaze. Surprisingly, we find that this is not a general property of face-selective regions: pRFs of face-selective regions of the lateral stream are both more peripheral and larger than those of the ventral stream. This finding requires a rethinking of spatial computations in face perception.

A substantial body of research[1,3,4] has highlighted differences in the computational goals of ventral and lateral streams: ventral regions are thought to be involved in static aspects of face perception such as face identification, while lateral regions are thought to be involved in dynamic[3,13,14] and transient[15] aspects of face perception such as expression[7,8] and gaze[18,19]. As such, the foveal bias of ventral face-selective regions has been attributed to the high visual acuity necessary for face identification, which is achieved by foveal vision[31]. Indeed, people tend to fixate on the center of the face during recognition[30,31,34], putting the VFC of ventral face selective regions on the internal face features that carry information about identity[34,53]. This raises the

468 question: what is the benefit of peripheral processing in the lateral stream? We propose a new
469 hypothesis: peripheral processing in lateral face-selective regions and direct white matter
470 connections between these regions to peripheral EVC may facilitate rapid processing of face
471 information. In-line with this prediction, behavioral studies show that (i) tasks associated with
472 the lateral stream such as face emotion judgements[27,53] or person recognition from dynamic face
473 and body stimuli[54] use peripheral information, and (ii) the speed of visual processing is faster in
474 the periphery[36]. Additionally, not only do lateral face-selective regions contain large and
475 peripheral pRFs, but they are also mainly driven by transient visual information[15]. Future studies
476 can test these hypotheses by measuring spatio-temporal pRFs, as well as behavioral performance
477 in the periphery for tasks related to the lateral stream.

478 Though dMRI is not capable of resolving whether the connections we find are
479 feedforward or feedback, the majority of connections in cortex are likely reciprocal[55]. Thus, we
480 conjecture that included in the white-matter connections we discovered are tracts that originate
481 in EVC and project to face-selective regions. Additionally, we do not intend to suggest that all
482 differences in spatial processing between ventral and lateral face-selective regions can be
483 attributed to direct connections with EVC. It is likely that hierarchical connections throughout the
484 ventral stream also contribute to shaping pRFs in face-selective regions, though we are not able
485 to resolve topographic information for these shorter connections with the present dMRI
486 resolution. Nonetheless, together with hierarchical connections, small differences in the
487 distribution of connections from EVC eccentricities to face-selective regions may result in
488 pronounced differences in spatial processing by pRFs across processing streams.

489 Our finding that visual field properties in face-selective regions are reflected in differential
490 white matter connections with EVC supports the idea that structural connections serve a
491 functional role. Our data suggest that it is not just that face-selective regions in different streams
492 use the input that they are receiving from early in the visual hierarchy differently, but that they
493 are actually receiving different input to begin with. Further, we hypothesize that white matter
494 connections between EVC and face-selective regions may explain higher functional connectivity
495 between ventral face-selective regions and central than peripheral eccentricities in EVC[56–58], a
496 prediction that can be tested in future research. As these functional connections are present

early in infancy[56], another important question for future research is whether these structural connections between EVC and downstream regions are present at birth and constrain where face-selective regions emerge during development[59].

Our results not only explicate the nature of connections between EVC and face-selective regions[41,42], but also substantially advance the precision with which we can understand connections within the human brain. In contrast to many dMRI studies that examine white matter connections of entire fascicles or between brain regions, to our knowledge this is the first study that identifies white matter connections associated with a topographic map in individual human brains. As receptive fields, topographic maps, and processing streams are key computational characteristics of sensory (e.g., audition[60]) and cognitive (e.g., numerosity[61]) brain systems and across species[52], our innovative approach can be applied to study how topographic computations emerge and are scaffolded by white matter connections in many brain systems and species.

In sum, we discovered differential spatial processing across face-selective regions in the ventral and lateral processing streams, which is mirrored by differences in white matter connections with eccentricity bands in EVC. These findings suggest a rethinking of computations in face-selective regions, and further propose that spatial processing in high-level regions may be scaffolded by the pattern of white matter connections from EVC.

515 **Methods**

516

517 **Participants**

518 Twenty-one participants (10 female, ages 22 to 45, mean age 27.1 ± 5.8 years) from Stanford University
519 participated in the study, sixteen of whom returned for diffusion MRI. All participants had normal or
520 corrected-to-normal vision. Participants gave informed consent and all procedures were approved by the
521 Stanford Internal Review Board on Human Subjects Research.

522

523 **MRI data acquisition**

524 Participants were scanned using a General Electric Discovery MR750 3T scanner located in the Center for
525 Cognitive and Neurobiological Imaging (CNI) at Stanford University. A phase-array 32-channel head coil
526 was used for all data acquisition except for the retinotopic mapping experiment (16-channel head coil).

527

528 *Anatomical Scans*

529 We obtained for each of 15 participants a whole-brain, anatomical volume using a T1-weighted BRAVO
530 pulse sequence (resolution: 1 mm x 1 mm x 1 mm, TI=450 ms, flip angle: 12°, 1 NEX, FoV: 240 mm). In 6
531 participants we used quantitative MRI measurements using the protocols from[62] to generate a 1 mm x 1
532 mm x 1 mm, T1-weighted anatomical image of their brain. Anatomical images of each participant's brain
533 were used for gray/white matter tissue segmentation, which was then used for cortical surface
534 reconstruction and visualization of data on the cortical surface.

535

536 *fMRI category localizer experiment:* A category localizer was run to identify voxels that responded more
537 strongly to one category vs. other categories of stimuli in order to localize face- and place-selective regions
538 of interest (ROIs). In the experiment, participants were presented with grayscale images of stimuli from
539 five domains, each with two categories (faces: child, adult; bodies: whole, limbs; places: corridors, houses;
540 characters: pseudowords, numbers; objects: cars, guitars) as described previously[45]. Images from each
541 category were presented in 4s trials at a rate of 2 Hz, intermixed with 4s blank trials. Each category was
542 shown eight times per run in counterbalanced order. Participants were instructed to fixate on a central
543 point and perform an oddball detection task, identifying 0-2 randomly presented phase scrambled images
544 within a trial. Runs were 318s long and each participant completed 3 runs with different images and
545 category order. Data were collected with a simultaneous multi-slice EPI sequence with a multiplexing
546 factor of 3 to acquire near whole-brain (48 slices) volumes at TR=1s, TE=30 ms at a resolution of 2.4 mm

547 isotropic. Data were acquired with a one-shot T2*-sensitive gradient echo sequence and slices were
548 aligned parallel to the parieto-occipital sulcus.
549
550 *pRF mapping experiment:* Each participant completed four runs of a wide-field pRF mapping experiment
551 to model the region of the visual field that elicits a response from each voxel (i.e. each voxel's pRF). In
552 each run, participants fixated on a central stimulus and were required to press a button whenever the
553 central fixation dot changed color as bars were swept across the screen (mean accuracy=95.2 $\pm$ 6.9%).
554 Due to our interest in higher-level category selective regions, bars of width 5.7° swept across high-
555 contrast, colorful, cartoon stimuli that spanned a wide-field circular aperture (40° x 40° of visual angle).
556 Images randomly changed at a rate of 8 Hz. In each run, bars of four orientations (0°, 45°, 90°, 135°) swept
557 the visual field in eight directions (2 opposite directions orthogonal to the bar orientation) with blanks
558 (mean luminance gray background with a fixation) interspersed at regular intervals. Each run lasted 3 min
559 and 24 s. Eye-tracking was not conducted in the scanner but visual field coverage of early visual field maps
560 (V1-V3) show the expected hemifields and quarterfields (**Figure 1B** for an example), indicating that
561 participants maintained stable fixation.
562
563 *Diffusion magnetic resonance imaging (dMRI):* In 16 of the participants, we acquired whole-brain
564 diffusion-weighted, dual-spin echo sequences (60 slices, TE=96.8 ms, TR=8,000 ms, 96 diffusion directions,
565 b0=2,000s/mm^2) at a resolution of 2.0 mm x 2.0 mm x 2.0 mm. Ten non-diffusion-weighted images were
566 collected at the beginning of each scan.
567
568 **Preprocessing and data analysis**
569 *Anatomical data:* T1-weighted images were automatically segmented using FreeSurfer 5.3
570 (https://surfer.nmr.mgh.harvard.edu/) and then manually validated and corrected using ITKGray
571 (http://web.stanford.edu/group/vista/cgi-bin/wiki/index.php/ItkGray). Using these segmentations, we
572 generated cortical surfaces in FreeSurfer.
573
574 *fMRI data analysis:* fMRI data analysis was performed in MATLAB (www.mathworks.com) and using the
575 mrVista analysis software (http://github.com/vistalab) developed at Stanford University. All data were
576 analyzed within the individual participants' native brain anatomy space without spatial smoothing. Data
577 were motion corrected within and between scans using mrVista motion correction algorithms, and then

manually aligned to the anatomical volume. The manual alignment was optimized using robust multiresolution alignment.

Definition of V1-V3 (EVC): V1, V2, and V3 were defined in all participants using their individual data from the pRF mapping experiment. Maps of pRF phase and eccentricity were projected onto an inflated cortical surface reconstruction for each participant and borders between the retinotopic maps were drawn on this cortical surface. The boundary was defined as the center of polar angle reversal occurring at the vertical or horizontal meridian[34]. V2 and V3 were drawn as quarterfields separated by V1 and were later combined to produce a hemifield representation. The early visual cortex (EVC) ROI was then defined as the union of V1, V2, and V3.

Definition of face-selective and place-selective functional regions of interest: The functional ROIs were defined in individual participants from the category localizer experiment using anatomical and functional criteria[45]. Statistical contrasts of faces > all other stimuli (for face-selective ROIs) and places > all other stimuli (for place-selective ROIs) were thresholded at t-values >3, voxel level, in each participant, as in previous work[34,45]. Face-selective ROIs were defined in the inferior occipital gyrus (IOG-faces, right hemisphere: *N*=20; left hemisphere: *N*=18), posterior fusiform gyrus (pFus-faces, right: *N*=18; left: *N*=18), mid fusiform gyrus (mFus-faces; right: *N*=17; left: *N*=19), posterior superior temporal sulcus (pSTS-faces, right: *N*=19; left: *N*=17), and medial superior temporal sulcus (mSTS-faces, right: *N*=18; left: *N*=9). An additional place-selective ROI was defined along the collateral sulcus (CoS-places, right: *N*=21; left: *N*=21), corresponding to the parahippocampal place area[63].

Estimating pRFs: We modeled the population receptive field (pRF) in each voxel using the compressive spatial summation (CSS) model[64]. Time course data was transformed from the functional slices to the T1-weighted anatomy using trilinear interpolation. We estimated pRFs within each gray matter voxel. The pRF model fits a 2-dimensional Gaussian for each voxel, with parameters x and y describing the location of the center of the pRF, and σ, the standard deviation of the Gaussian in degrees of visual angle. An additional compressive summation exponent (n) is fit for each voxel to capture the nonlinear summation properties of pRFs in later stages of the visual hierarchy[26,64]. We define the size of the pRF as $\sigma/\mathrm{sqrt}(n)$[64]. Candidate pRFs are estimated and a predicted time-series is produced by convolving the product of the binarized stimulus sequence and the candidate pRF with an HRF. The model parameters x, y, and σ, are then iteratively adjusted to minimize the sum of squared errors between the predicted time-series and

610 the observed time-series. Phase (atan(y/x)) and eccentricity (sqrt($x^2 + y^2$) of each voxel are derived from
611 the x and y coordinates of the pRF center to generate phase and eccentricity maps respectively. Voxels
612 were included for subsequent analysis if the variance explained by the pRF model was greater than 10%.
613 Additionally, to ensure accurate pRF fits by the optimization procedure, voxels whose σ remained at the
614 initial minimum value (0.21°) were excluded from further analysis. For analyses of pRFs in each ROI, we
615 include data from participants for whom the ROI was identified and at least 25 voxels (corresponding to
616 a volume of $\geq$ 25 mm^3) of the ROI were retinotopically modulated according to the above criteria
617 (variance explained ≥10%, pRF size > 0.21°). The number of participants per ROI is as follows: IOG-faces,
618 right hemisphere *N*=19, left *N*=17; pFus-faces, right *N*=18, left *N*=18; mFus-faces, right *N*=17, left *N*=17;
619 pSTS-faces, right *N*=16, left *N*=13; mSTS-faces, right *N*=6, left *N*=2; CoS-places, right *N*=21, left *N*=21. Note
620 that left mSTS-faces in not included in further analyses as we were only left with two participants.
621
622 *Visual field coverage (VFC):* is defined as the portion of the visual field that is processed by the set of pRFs
623 spanning the ROI. To calculate the VFC for a given ROI and participant, all voxels in an ROI that passed the
624 above inclusion criteria are included. Each pRF is modeled with a binary circular mask centered at the pRF
625 center and with a diameter of $2\sigma/\sqrt{n}$. For each location in the visual field, the VFC value is the pRF density
626 at that location. Group average VFC maps are created by averaging the individual VFC maps for that ROI.
627 Thus, the group VFC depicts the mean pRF density at each location averaged across subjects. To assess
628 differences in VFC across ROIs, we fitted a line relating pRF density to eccentricity in each ROI and
629 participant, and then compared the average slopes (across participants) of different ROIs in each stream.
630 Linear fits were chosen over more complicated models as the linear model fit (R^2) was high for all ROIs
631 (right: mean R^2s > 0.71, left: mean R^2s > 0.66)
632 For each functional ROI, we also calculated indices of contra- vs. ipsi-laterality and upper vs. lower
633 visual field bias of the VFC (**Supplementary Figure S3**). Laterality of VFC was calculated for each participant
634 and ROI as the mean coverage in the contralateral visual field minus the mean coverage in the ipsilateral
635 visual field, divided by the sum of the two ($\frac{contra - ipsi}{contra + ipsi}$). Similarly, the upper field bias for each participant
636 and ROI was quantified as the average coverage in the contralateral upper visual field minus the average
637 coverage in the contralateral lower visual field, divided by the sum of the two ($\frac{upper - lower}{upper + lower}$).
638
639 *dMRI data analysis:* dMRI data were preprocessed using a combination of tools from MRtrix3[65], ANTs, and
640 FSL, as in[66,67]. We denoised the data using: (i) a principal component analysis, (ii) Rician based denoising,

641 and (iii) Gibbs ringing corrections[68]. We also corrected for eddy currents and motion using FSL and
642 performed bias correction using ANTs. The dMRI data were then registered to the average of the non-
643 diffusion-weighted images and aligned to the corresponding anatomical brain volume of the participant
644 using rigid body transformation. We used constrained spherical deconvolution[65] with up to eight spherical
645 harmonics (lmax=8) to calculate the voxel-wise tract orientation distributions (FOD). These FODs were
646 then used for tractography.
647
648 *Tractography:* Ensemble tractography[69] with linear fascicle evaluation (LiFE[70]) was performed using the
649 preprocessed dMRI data and consisted of 3 main steps:
650 1) We used MRtrix3[65] to generate five candidate connectomes which varied in the maximum angle
651 (2.9°, 5.7°, 11.5°, 23.1°, and 47.2°). Each candidate connectome was seeded on the gray white
652 matter interface (GWMI) using anatomically constrained tractography (ACT[51]) and consisted of
653 500,000 streamlines. This approach allows us to generate multiple connectomes with different
654 degrees of curvature, as opposed to restricting our estimations to a single connectome with one
655 particular set of parameters[69]. Each candidate connectome was generated using probabilistic
656 tract tracking with the following parameters: algorithm: IFOD2, step size: 1 mm, minimum length:
657 4 mm, maximum length: 200 mm. ACT[51] uses the GWMI from the FreeSurfer segmentation of
658 each participant's brain to seed the tracking algorithm. This enabled us to focus only on those
659 fiber tracts that reach the gray matter.
660 2) The five candidate connectomes were concatenated into one ensemble connectome containing
661 a total of 2,500,000 streamlines.
662 3) We used linear fascicle evaluation (LiFE[70]) to validate the ensemble connectome. LiFE was used to
663 determine which fiber estimates make a significant contribution to predicting the dMRI data and
664 removes false alarm tracts that did not significantly contribute to predicting the dMRI data.
665
666 *Functionally defined white matter tracts (FDWT):* To determine the white matter tracts that are associated
667 with each functional ROI, we intersected the tracts with the GWMI directly adjacent to each functional
668 ROI for each participant. This yielded functionally defined white matter tracts (FDWT) for each face and
669 place-selective ROI.
670 EVC-fROI connections: To identify tracts connecting these functional ROIs and early visual cortex, we
671 intersected the FDWM of the fROI with the GWMI underneath EVC (union of V1, V2, V3), and then used
672 these pairwise tracts for individual subject visualization and endpoint density estimation.

673 *Quantification of endpoint density*

674 We used MRtrix3[65] and track-density imaging (TDI) to create tract maps of the streamline endpoints of
675 the FDWT for each functional ROI. These endpoint density maps were transformed to the cortical surface
676 using FreeSurfer. We examined the portion of the endpoint density maps that intersected EVC and
677 determined the corresponding eccentricity values. Eccentricity was derived from the pRF mapping
678 experiment and each participant's individual retinotopic maps. We used the track-density values to weight
679 each eccentricity value based on the density of endpoints connecting to that eccentricity. We then
680 quantified the proportion of endpoints in each of four eccentricity bands (0° to 5°, 5° to 10°, 10° to 20°,
681 20° to 40°) for each fROI and participant separately.

682

683 *Size control*: As functional ROIs vary in size across participants and regions, we did a control analysis to
684 evaluate the endpoint density using constant-size spherical ROIs (radius=5mm) centered on each
685 participant's functional ROIs. The goal of this analysis was to test whether differences across ROIs could
686 be attributed to differences in ROI size. Results of these analyses are presented in the Supplementary
687 Materials (**Supplementary Figure S5**).

688

689 **Statistical analyses**

690 Statistical analyses were computed using the *lmerTest*[48] and *lsmeans* packages in R (https://cran.r-
691 project.org/web/packages/lmerTest/, https://cran.r-project.org/web/packages/lsmeans/). Linear mixed-
692 effects models (LMMs) were used for statistical analyses because our data includes missing data points
693 (not all participants have all ROIs). LMMs were constructed separately for each hemisphere, with one
694 exception: to test the effect of hemisphere on the proportion of pRF centers by eccentricity band in the
695 ventral face-selective ROIs (i.e. to test the lateralization of the foveal bias), we constructed an LMM which
696 can be expressed as: *proportion of pRF centers ~ eccentricity band + ROI + hemisphere + (eccentricity*
697 *band*ROI) + (ROI*hemisphere) + (eccentricity band*hemisphere) + (eccentricity band*ROI*hemisphere) +*
698 *(1|subject).* The significance of LMM model terms was evaluated using repeated-measures analyses-of-
699 variance (LMM ANOVAs; type III), with Satterthwaite's method of correction for degrees of freedom[47].
700 Post-hoc tests were done by computing Tukey's Honest Significant Difference (HSD) where the family-
701 wise confidence level is set at 0.95. p-values reported from these post-hoc tests are thus corrected for
702 multiple comparisons. All statistical tests conducted in the manuscript followed this procedure other than
703 two paired t-tests. One paired t-test was conducted to compare the average pRF size across streams
704 (average pRF size across ventral ROIs vs. average pRF size across lateral ROIs) and one was conducted to

compare slopes of the pRF density by eccentricity lines across streams (average slope across ventral ROIs vs. average slope across lateral ROIs).

Data and code availability

fMRI data were analyzed using the open source mrVista software package (available on GitHub: http://github.com/vistalab). T1-weighted anatomicals for six subjects were generated using the mrQ software package (https://github.com/mezera/mrQ). dMRI data were analyzed using mrTrix3 (http://www.mrtrix.org/). Custom code (all available on GitHub) was used for dMRI preprocessing (https://github.com/vistalab/RTP-preproc; https://github.com/vistalab/RTP-pipeline) and processing of the pRF experiment (https://github.com/VPNL/toonotopy). Code for all further analysis, including reproducing all figures and statistics, can be found at https://github.com/VPNL/fibeRFs. Processed data is additionally available at https://github.com/VPNL/fibeRFs while the individual nifti files are available upon request.

718 **References**

719 1. Haxby, J. V, Hoffman, E. a & Gobbini, M. I. The distributed human neural system for face
720 perception [Record Supplied By Publisher]. *Trends Cogn Sci* (2000). doi:10.1016/S1364-
721 6613(00)01482-0
722 2. Weiner, K. S. & Grill-Spector, K. Neural representations of faces and limbs neighbor in
723 human high-level visual cortex: Evidence for a new organization principle. *Psychol. Res.*
724 **77**, 74–97 (2013).
725 3. Duchaine, B. & Yovel, G. A Revised Neural Framework for Face Processing. *Annu. Rev. Vis.*
726 *Sci.* (2015). doi:10.1146/annurev-vision-082114-035518
727 4. Freiwald, W., Duchaine, B. & Yovel, G. Face Processing Systems: From Neurons to Real-
728 World Social Perception. *Annu. Rev. Neurosci.* (2016). doi:10.1146/annurev-neuro-
729 070815-013934
730 5. Kanwisher, N., McDermott, J. & Chun, M. M. The fusiform face area: a module in human
731 extrastriate cortex specialized for face perception. *J. Neurosci.* **17**, 4302–4311 (1997).
732 6. Grill-Spector, K., Knouf, N. & Kanwisher, N. The fusiform face area subserves face
733 perception, not generic within-category identification. *Nat. Neurosci.* **7**, 555–562 (2004).
734 7. Andrews, T. J. & Ewbank, M. P. Distinct representations for facial identity and changeable
735 aspects of faces in the human temporal lobe. *Neuroimage* (2004).
736 doi:10.1016/j.neuroimage.2004.07.060
737 8. Winston, J. S., Henson, R. N. A. A., Fine-Goulden, M. R. & Dolan, R. J. fMRI-adaptation
738 reveals dissociable neural representations of identity and expression in face perception.
739 *J. Neurophysiol.* (2004). doi:10.1152/jn.00155.2004
740 9. Pitcher, D., Walsh, V., Yovel, G. & Duchaine, B. TMS Evidence for the Involvement of the
741 Right Occipital Face Area in Early Face Processing. *Curr. Biol.* **17**, 1568–1573 (2007).
742 10. Gauthier, I., Skudlarski, P., Gore, J. C. & Anderson, A. W. Expertise for cars and birds
743 recruits brain areas involved in face recognition. *Nat. Neurosci.* **3**, 191–197 (2000).
744 11. Weiner, K. S. & Grill-Spector, K. *The evolution of face processing networks*. *Trends in*
745 *Cognitive Sciences* (2015). doi:10.1016/j.tics.2015.03.010
746 12. Pyles, J. A., Verstynen, T. D., Schneider, W. & Tarr, M. J. Explicating the Face Perception

Network with White Matter Connectivity. *PLoS One* **8**, e61611 (2013).

13. Fox, C. J., Iaria, G. & Barton, J. J. S. Defining the face processing network: Optimization of the functional localizer in fMRI. *Hum. Brain Mapp.* (2009). doi:10.1002/hbm.20630

14. Pitcher, D., Dilks, D. D., Saxe, R. R., Triantafyllou, C. & Kanwisher, N. Differential selectivity for dynamic versus static information in face-selective cortical regions. *Neuroimage* **56**, 2356–2363 (2011).

15. Stigliani, A., Jeska, B. & Grill-Spector, K. Differential sustained and transient temporal processing across visual streams. *PLoS Comput. Biol.* (2019). doi:10.1371/journal.pcbi.1007011

16. Puce, A., Allison, T., Bentin, S., Gore, J. C. & McCarthy, G. Temporal cortex activation in humans viewing eye and mouth movements. *J. Neurosci.* **18**, 2188–99 (1998).

17. Pitcher, D., Duchaine, B. & Walsh, V. Combined TMS and fMRI reveal dissociable cortical pathways for dynamic and static face perception. *Curr. Biol.* **24**, 2066–2070 (2014).

18. Calder, A. J. *et al.* Separate Coding of Different Gaze Directions in the Superior Temporal Sulcus and Inferior Parietal Lobule. *Curr. Biol.* (2007). doi:10.1016/j.cub.2006.10.052

19. Carlin, J. D. & Calder, A. J. The neural basis of eye gaze processing. *Current Opinion in Neurobiology* (2013). doi:10.1016/j.conb.2012.11.014

20. Pitcher, D., Walsh, V. & Duchaine, B. The role of the occipital face area in the cortical face perception network. *Exp. Brain Res.* (2011). doi:10.1007/s00221-011-2579-1

21. Huk, A. C., Dougherty, R. F. & Heeger, D. J. Retinotopy and functional subdivision of human areas MT and MST. *J. Neurosci.* (2002). doi:20026661

22. Grossman, E. D. & Blake, R. Brain Areas Active during Visual Perception of Biological Motion. *Neuron* **35**, 1167–1175 (2002).

23. Beauchamp, M. S., Lee, K. E., Haxby, J. V. & Martin, A. Parallel visual motion processing streams for manipulable objects and human movements. *Neuron* (2002). doi:10.1016/S0896-6273(02)00642-6

24. Hubel, D. H. & Wiesel, T. N. Receptive fields and functional architecture in two nonstriate visual areas (18 And 19) of the cat. *J Neurophysiol* **28**, 229–289 (1965).

25. Dumoulin, S. O. & Wandell, B. A. Population receptive field estimates in human visual

776 cortex. *Neuroimage* **39**, 647–660 (2008).
777 26. Kay, K. N., Weiner, K. S. & Grill-Spector, K. Attention reduces spatial uncertainty in
778 human ventral temporal cortex. *Curr. Biol.* **25**, 595–600 (2015).
779 27. Pelphrey, K. A. *et al.* Visual Scanning of Faces in Autism. *J. Autism Dev. Disord.* (2002).
780 doi:10.1023/A:1016374617369
781 28. Hsiao, J. H. W. & Cottrell, G. Two fixations suffice in face recognition. *Psychol. Sci.* (2008).
782 doi:10.1111/j.1467-9280.2008.02191.x
783 29. van Belle, G., Ramon, M., Lefèvre, P. & Rossion, B. Fixation patterns during recognition of
784 personally familiar and unfamiliar faces. *Front. Psychol.* (2010).
785 doi:10.3389/fpsyg.2010.00020
786 30. Peterson, M. F. & Eckstein, M. P. Looking just below the eyes is optimal across face
787 recognition tasks. *Proc. Natl. Acad. Sci. U. S. A.* (2012). doi:10.1073/pnas.1214269109
788 31. Malach, R., Levy, I. & Hasson, U. The topography of high-order human object areas.
789 *Trends Cogn Sci* **6**, 176–184 (2002).
790 32. Hasson, U., Levy, I., Behrmann, M., Hendler, T. & Malach, R. Eccentricity bias as an
791 organizing principle for human high-order object areas. *Neuron* **34**, 479–490 (2002).
792 33. Levy, I. *et al.* Center-periphery organization of human object areas. *Nat. Neurosci.* (2001).
793 doi:10.1038/87490
794 34. Gomez, J., Natu, V., Jeska, B., Barnett, M. & Grill-Spector, K. Development differentially
795 sculpts receptive fields across early and high-level human visual cortex. *Nat. Commun.* **9**,
796 788 (2018).
797 35. Behrmann, M. & Plaut, D. C. A vision of graded hemispheric specialization. *Ann. N. Y.*
798 *Acad. Sci.* **1359**, 30–46 (2015).
799 36. Carrasco, M., McElreel, B., Denisova, K. & Giordano, A. M. Speed of visual processing
800 increases with eccentricity. *Nat. Neurosci.* (2003). doi:10.1038/nn1079
801 37. Azzopardi, P. & Cowey, A. Preferential representation of the fovea in the primary visual
802 cortex. *Nature* (1993). doi:10.1038/361719a0
803 38. Jiang, X. *et al.* Evaluation of a Shape-Based Model of Human Face Discrimination Using
804 fMRI and Behavioral Techniques. *Neuron* (2006). doi:10.1016/j.neuron.2006.03.012

39. Yamins, D. L. K. *et al.* Performance-optimized hierarchical models predict neural responses in higher visual cortex. *Proc. Natl. Acad. Sci.* (2014). doi:10.1073/pnas.1403112111

40. Grill-Spector, K., Weiner, K. S., Kay, K. N. & Gomez, J. The Functional Neuroanatomy of Human Face Perception. *Annu. Rev. Vis. Sci.* **3**, 167–196 (2017).

41. Gschwind, M., Pourtois, G., Schwartz, S., Van De Ville, D. & Vuilleumier, P. White-matter connectivity between face-responsive regions in the human brain. *Cereb. Cortex* **22**, 1564–1576 (2012).

42. Weiner, K. S. *et al.* The face-processing network is resilient to focal resection of human visual cortex. *J. Neurosci.* **36**, 8425–8440 (2016).

43. Rossion, B., Dricot, L., Goebel, R. & Busigny, T. Holistic face categorization in higher order visual areas of the normal and prosopagnosic brain: Toward a non-hierarchical view of face perception. *Front. Hum. Neurosci.* (2011). doi:10.3389/fnhum.2010.00225

44. Stigliani, A., Jeska, B. & Grill-Spector, K. Encoding model of temporal processing in human visual cortex. *Proc. Natl. Acad. Sci. U. S. A.* **114**, E11047-E11056; (2017).

45. Stigliani, A., Weiner, K. S. & Grill-Spector, K. Temporal processing capacity in high-level visual cortex is domain specific. *J. Neurosci.* **35**, 12412–12424 (2015).

46. Song, S. *et al.* Local but not long-range microstructural differences of the ventral temporal cortex in developmental prosopagnosia. *Neuropsychologia* (2015). doi:10.1016/j.neuropsychologia.2015.10.010

47. Luke, S. G. Evaluating significance in linear mixed-effects models in R. *Behav. Res. Methods* (2017). doi:10.3758/s13428-016-0809-y

48. Kuznetsova, A., Brockhoff, P. B. & Christensen, R. H. B. lmerTest Package: Tests in Linear Mixed Effects Models . *J. Stat. Softw.* (2017). doi:10.18637/jss.v082.i13

49. Wandell, B. A. & Winawer, J. Computational neuroimaging and population receptive fields. **19**, 349–357 (2015).

50. Barton, B. & Brewer, A. A. Visual field map clusters in high-order visual processing: Organization of V3a/V3B and a new cloverleaf cluster in the posterior superior temporal sulcus. *Front. Integr. Neurosci.* (2017). doi:10.3389/fnint.2017.00004

834 51. Smith, R. E., Tournier, J.-D., Calamante, F. & Connelly, A. Anatomically-constrained
835 tractography: Improved diffusion MRI streamlines tractography through effective use of
836 anatomical information. *Neuroimage* **62**, 1924–1938 (2012).
837 52. Janssens, T., Zhu, Q. Q., Popivanov, I. D. & Vanduffel, W. Probabilistic and Single-Subject
838 Retinotopic Maps Reveal the Topographic Organization of Face Patches in the Macaque
839 Cortex. *J. Neurosci.* (2014). doi:10.1523/JNEUROSCI.2914-13.2013
840 53. Gosselin, F. & Schyns, P. G. Bubbles: A technique to reveal the use of information in
841 recognition tasks. *Vision Res.* (2001). doi:10.1016/S0042-6989(01)00097-9
842 54. O'Toole, A. J. *et al.* Recognizing people from dynamic and static faces and bodies:
843 Dissecting identity with a fusion approach. *Vision Res.* (2011).
844 doi:10.1016/j.visres.2010.09.035
845 55. Felleman, D. J. & Van Essen, D. C. Distributed hierarchical processing in the primate
846 cerebral cortex. *Cereb. Cortex* (1991). doi:10.1093/cercor/1.1.1
847 56. Arcaro, M. J. & Livingstone, M. S. A hierarchical, retinotopic proto-organization of the
848 primate visual system at birth. *Elife* **6**, (2017).
849 57. Butt, O. H., Benson, N. C., Datta, R. & Aguirre, G. K. The Fine-Scale Functional Correlation
850 of Striate Cortex in Sighted and Blind People. *J. Neurosci.* (2013).
851 doi:10.1523/JNEUROSCI.0363-13.2013
852 58. Arcaro, M. J., Honey, C. J., Mruczek, R. E. E. B., Kastner, S. & Hasson, U. Widespread
853 correlation patterns of fMRI signal across visual cortex reflect eccentricity organization.
854 *Elife* **4**, (2015).
855 59. Saygin, Z. M. *et al.* Anatomical connectivity patterns predict face selectivity in the
856 fusiform gyrus. *Nat. Neurosci.* **15**, 321–327 (2012).
857 60. Formisano, E. *et al.* Mirror-symmetric tonotopic maps in human primary auditory cortex.
858 *Neuron* (2003). doi:10.1016/S0896-6273(03)00669-X
859 61. Harvey, B. M., Klein, B. P., Petridou, N. & Dumoulin, S. O. Topographic representation of
860 numerosity in the human parietal cortex. *Science (80-.).* (2013).
861 doi:10.1126/science.1239052
862 62. Mezer, A. *et al.* Quantifying the local tissue volume and composition in individual brains

with magnetic resonance imaging. *Nat. Med.* **19**, (2013).

63. Epstein, R. & Kanwisher, N. A cortical representation the local visual environment. *Nature* (1998). doi:10.1038/33402

64. Kay, K. N., Winawer, J., Mezer, A. & Wandell, B. A. Compressive spatial summation in human visual cortex. *J. Neurophysiol.* **110**, 481–494 (2013).

65. Tournier, J. D. *et al.* MRtrix3: A fast, flexible and open software framework for medical image processing and visualisation. *NeuroImage* (2019). doi:10.1016/j.neuroimage.2019.116137

66. Lerma-Usabiaga, G., Mukherjee, P., Ren, Z., Perry, M. L. & Wandell, B. A. Replication and generalization in applied neuroimaging. *Neuroimage* (2019). doi:10.1016/j.neuroimage.2019.116048

67. Grotheer, M., Zhen, Z., Lerma-Usabiaga, G. & Grill-Spector, K. Separate lanes for adding and reading in the white matter highways of the human brain. *Nat. Commun.* (2019). doi:10.1038/s41467-019-11424-1

68. Veraart, J. *et al.* Denoising of diffusion MRI using random matrix theory. *Neuroimage* (2016). doi:10.1016/j.neuroimage.2016.08.016

69. Takemura, H., Caiafa, C. F., Wandell, B. A. & Pestilli, F. Ensemble Tractography. *PLoS Comput. Biol.* **12**, e1004692 (2016).

70. Pestilli, F., Yeatman, J. D., Rokem, A., Kay, K. N. & Wandell, B. A. Evaluation and statistical inference for human connectomes. *Nat. Methods* **11**, 1058–1063 (2014).

Acknowledgements

This work was supported by a William R. and Sara Hart Kimball Stanford Graduate Fellowship awarded to DF; NIH grants (grant numbers 1RO1EY02231801, 1RO1EY02391501 to KGS); an NIH training grant (grant number 5T32EY020485 to VN); Ruth L. Kirschstein National Research Service Award (grant number F31EY027201 to JG) and the NSF Graduate Research Development Program (grant number DGE-114747 to JG).

892 **Author contributions**

893 D.F. designed the experiment, collected data, analyzed the data, and wrote the manuscript.

894 J.G. collected the data, contributed to data analysis and contributed to the manuscript.

895 M.N., and A.A.R., collected the data, and contributed to the manuscript.

896 S.P. contributed to data analysis and contributed to the manuscript.

897 K.G-S. designed the experiment, contributed to the data analysis, and wrote the manuscript.